Journal of
Ceramic Science
and Technology

J. Ceram. Sci. Technol., **09** [3] 289-300 (2018)
DOI: 10.4416/JCST2018-00017
available online at: http://www.ceramic-science.com

Influence of Reaction-Sintering and Calcination Conditions on Thermoelectric Properties of Sm-doped Calcium Manganate $CaMnO_3$

S. Bresch*[1], B. Mieller[1], F. Delorme[2], C. Chen[2], M. Bektas[3], R. Moos[3], T. Rabe[1]

[1]Advanced Technical Ceramics Division, Bundesanstalt für Materialforschung und -prüfung (BAM), Unter den Eichen 44 – 46, D-12203 Berlin, Germany
[2]Université de Tours, CNRS, CEA, INSA CVL, GREMAN UMR 7347, IUT de Blois, 15 rue de la chocolaterie, CS 2903, 41029 Blois Cedex, France
[3]Department of Functional Materials, University of Bayreuth, Universitätsstraße 30, D-95447 Bayreuth, Germany

received February 28, 2018; received in revised form June 18, 2018; accepted June 27, 2018

Abstract

A wide range of solid-state synthesis routes for calcium manganate is reported in the literature, but there is no systematic study about the influence of the solid-state synthesis conditions on thermoelectric properties. Therefore, this study examined the influence of calcination temperature and calcination cycles on the Seebeck coefficient, electrical conductivity, and thermal conductivity. Higher calcination temperatures and repeated calcination cycles minimized the driving force for sintering of the synthesized powder, leading to smaller shrinkage and lower densities of the sintered specimens. As the electrical conductivity increased monotonously with increasing density, a higher energy input during calcination caused deterioration of electrical conductivity. Phase composition and Seebeck coefficient of sintered calcium manganate were not influenced by the calcination procedure. The highest thermoelectric properties with the highest power factors and figures of merit were obtained by means of reaction-sintering of uncalcined powder.

Keywords: Thermoelectric oxides, calcination, solid-state-synthesis, power factor, reaction-sintering

I. Introduction

Thermoelectric energy conversion is a promising energy harvesting technology that has attracted much interest lately [1–4]. With the Seebeck effect, a temperature gradient is directly transformed into a voltage. Besides a high Seebeck coefficient S, thermoelectric materials should also have high electrical conductivity σ and low thermal conductivity κ. The higher the power factor PF and the figure of merit ZT are, the more efficient is the conversion of thermal into electrical energy.

$$ZT = \frac{S^2 \cdot \sigma}{\kappa} T = \frac{PF}{\kappa} T \qquad (1)$$

Common thermoelectric materials like tellurides may start to decompose at temperatures above 300 °C. Oxide thermoelectric materials are an interesting alternative for high-temperature applications, albeit their PF and ZT are much lower than respective values of telluride compounds. Many thermoelectric oxides are stable in air up to at least 900 °C. Their raw materials are often less toxic and more abundant compared to tellurides [5].

Promising n-type thermoelectric oxides are doped $SrTiO_3$ [6,7], doped ZnO [8–10], and doped $CaMnO_3$ [1,11]. $CaMnO_3$ has attracted a lot of attention in recent years as it exhibits favourable high thermoelectric properties, a high temperature stability even in oxidizing atmospheres, and it can be synthesized from inexpensive raw materials. $CaMnO_3$ is a perovskite with an orthorhombic crystal structure at room temperature that changes to tetragonal at 896 °C and to cubic at 913 °C [12]. Undoped $CaMnO_3$ has a very high absolute value for the Seebeck coefficient $|S|$ of about |-350 µV/K| at room temperature [11,13], but exhibits only low electrical conductivity between 10 S/m [11] and 1000 S/m [13] at room temperature. To increase the electrical conductivity, $CaMnO_3$ can be doped with different lanthanides like Gd [13], Yb [14], or Sm [11], and elements from group III to V of the periodic table [11] on the Ca-site; and with penta- and hexavalent transition metals [15,16] on the Mn-site to create Mn^{3+} in a matrix of Mn^{4+}. As shown by Ohtaki [11] for A-site doping with Bi, Sm, La and Pb; by Bhaskar [13] for A-site doping with Dy; and by Reimann [17] for co-doping with Gd at the A-site and Wo at the B-site, the increased charge carrier concentration increases the electrical conductivity but also leads to a moderate decline of $|S|$. Nevertheless, the power factor PF increases as the increase in electrical conductivity overcompensates the decrease in $|S|$ up to 600 °C [11,13,17]. Samarium is an example of effective Ca-site doping. It leads to power factor values between 80 µW/K²m and 160 µW/K²m at room temperature [11,13,18,19] (for doping levels between 0.02 mol and 0.1 mol) and between 160 µW/K²m and 200 µW/K²m

* Corresponding author: sophie.bresch@bam.de

at 600 °C [11,19] (for doping levels between 0.05 mol and 0.1 mol). The dimensionless figure of merit amounts to values between 0.01 and 0.02 at room temperature [13,18] and to 0.03 at 600 °C [13].

In thermoelectric generators, doped $CaMnO_3$ is often used in combination with doped $Ca_3Co_4O_9$ as p-type material [20–22]. Koumoto *et al.* reported an output power of 12 W generated by a 10 cm² module at $\Delta T = 400$ K with 800 °C at the hot side, using a $CaMnO_3$ with a ZT (700 °C) = 0.16 [22]. Reimann *et al.* [23] used doped $CaMnO_3$ with a ZT (700 °C) = 0.03 in a transversal unileg thermoelectric generator, which generated 13 mW at a $\Delta T = 200$ K and 300 °C at the hot side. An output power of 30 mW is already sufficient to run a small sensor system [24].

The two main powder synthesis routes for $CaMnO_3$ are soft chemistry and solid-state reaction, the latter historically also known as the mixed-oxides route. For both synthesis routes, the final phase is formed during a thermal process known as calcination. Co-precipitation of carbonates [2,18] and the citrate route [2,20] are the most commonly used soft-chemistry approaches. After a calcination step at 800 °C [18] or 900 °C [2,20], these processes lead to nano-sized powders and a very good microstructural homogeneity, especially concerning the distribution of dopants as shown recently by Löhnert *et al.* [2]. The high surface area of nano-sized particles increases the driving force for sintering, which leads to higher sinter densities and increased electrical conductivities. Compared to the solid-state synthesis, soft chemistry methods are costlier owing to the more expensive raw materials [25].

The mixed oxide route, in contrast, is not only cost-effective but also easily scalable with the use of rotary kilns. Therefore, it is widely used to produce various electroceramic materials like PZT and $BaTiO_3$ on industrial scale [26]. For calcium manganate $CaMnO_3$, a wide range of synthesis conditions is described in literature [2, 5, 11, 13, 16, 19, 27–30]. Most authors used $CaCO_3$ and manganese oxides like MnO or MnO_2 as raw materials [13, 16, 27–30]. In some cases, $MnCO_3$ was used [11,19]. The raw materials were either dry-milled in a planetary ball mill for a long time [11,27] (up to 11 days [29]) or wet-milled with zirconia balls in propan-2-ol for 6 h [2] or 24 h [16], respectively. These mixtures were then calcined at 850 °C [11,29], 900 °C [19, 27, 28], 1 000 °C [30] or 1 100 °C [2, 16] for 4 h[16], 12 h [28, 30], or up to 24 h [19, 27]. In some cases, the calcination was repeated at the same temperature [16] or at 200 K higher temperatures [30] with an intermediate grinding step. Löhnert *et al.* [2] fine-milled the calcined powder for several hours to obtain nano-sized powders.

Although the solid-state synthesis is a high-temperature process with long dwell times and sometimes several cycles, only very few authors studied the influence of the synthesis conditions on the thermoelectric properties systematically. Berbenni *et al.* [29] investigated the influence of high-energy ball milling of the raw materials on the phase composition after calcination. They showed that high-energy ball milling leads to a solid solution of the raw materials. After calcination at 900 °C, $CaMnO_3$ was synthesized. In contrast, a physical mixture without mechanical impact on the particles did not lead to a complete synthesis of $CaMnO_3$, even at 1 000 °C. Thermoelectric properties were not studied. Kabir *et al.* [14] varied the particle size of the calcined powder from $d_{50} = 15$ µm to $d_{50} = 1.5$ µm by adjusting the milling time. They showed that a smaller particle size increases the relative sinter density from 67 % to 98 % after sintering at 1250 °C for 10 h. A bigger particle size resulted in higher resistivity (factor 2) and higher $|S|$ (+ 13 %). As the sinter density increased with longer milling times, the thermal conductivity increased as well (from 1.5 W/mK to 2.6 W/mK). A recent study [31] on the influence of the solid-state synthesis conditions on the thermoelectric properties of $Ca_3Co_4O_9$, a p-type material, showed that a lower energy input during calcination (like lower temperatures, shorter dwell time and fewer cycles) increased the sinter density and the *PF*. The highest *PF* was reached for uncalcined, reaction-sintered $Ca_3Co_4O_9$.

Here, we present a systematic study on the influence of calcination temperature and number of cycles on the thermoelectric properties of $CaMnO_3$. To the best of the authors' knowledge, no such study has been published as yet.

II. Experimental

(1) Sample preparation

Stoichiometric amounts of calcium carbonate (99 %, low-alkali, Riedel-de Haën), manganese carbonate (≥ 99.9 %, Aldrich Chemistry), and samarium hydroxide (99.9 %, Alfa-Ventron) were weighed to obtain $Ca_{0.98}Sm_{0.02}MnO_3$ after sintering. 120 g of the mixture were attrition-milled (moliNEx, Netzsch) with 1300 g of zirconia grinding media ($d = 2…3$ mm) in 140 g of ethanol for 45 min at 800 rpm. Afterwards, the ethanol was evaporated in a rotary evaporator (Rotavapor R-124, Büchi). To investigate the influence of the calcination temperature, the mixture was calcined in alumina crucibles at 850 °C or at 1050 °C for 2 h twice with a heating rate of 5 K/min, respectively. The calcined powder was dry-milled after each calcination cycle in agate grinding bowls with agate grinding media in a planetary ball mill (Pulverisette 5, Fritsch) for 15 min with a rotation speed of 215 rpm. The influence of the calcination cycles was analysed based on preparation of an uncalcined powder mixture, a mixture that was calcined once at 850 °C and another mixture that was calcined twice at 850 °C. Aqueous solutions with 1.5 wt% of pressing additives (Zusoplast 9002 and Optapix AC 95, Zschimmer & Schwarz) were mixed to the calcined powders. After drying, the densely packed powder-binder mixtures were ground into ready-to-press flakes (sieved on a 200 µm sieve). From the flakes of each composition, different specimens were uniaxially pressed with 30 MPa and then sintered at 1250 °C for 2 h in air with a heating rate of 1 K/min from 850 °C to 950 °C and 5 K/min for the remaining temperature range. The following specimen dimensions were sintered: five test bars with the dimensions of 50 mm × 5 mm × 5 mm to determine the thermoelectric and physical properties at room temperature; discs with a diameter of 25 mm and a thickness after sintering of 1 mm. From these sintered discs, square samples with an edge

length of 6 mm (for thermal conductivity) and bars with a length of 15 mm and a width of 3 mm (for power factor measurements at elevated temperatures) were cut out.

(2) Characterization

The decomposition and reaction of the raw materials were analysed by means of thermo-gravimetric analysis (TAG24, Setaram) coupled with mass spectroscopy (Thermostar, Balzers). The measurements were conducted in air with a heating rate of 5 K/min up to a maximum temperature of 1200 °C in alumina crucibles.

The particle sizes of the powders were determined by means of laser powder diffraction (Mastersizer 2000, Malvern Instruments) after each milling step. The dimensions of the test bars (height h, width w and length l) were determined before and after sintering with a micrometre gauge, and the weight (m) with an analytical balance (resolution = 0.1 mg). The linear shrinkage dl/l_0 was calculated according to

$$dl/l_0 = \frac{l_0 - l_1}{l_0} \cdot 100\% \qquad (2).$$

In Equation (2), l_0 denotes the length before sintering and l_1 the length after sintering. The apparent density ρ was determined by means of the Archimedes method using Equation (3) with the density of water ρ_w, the dry mass of specimen m_1, the apparent mass under water of specimen m_2, and the soaked mass of specimen m_3.

$$\rho = \rho_w \frac{m_1}{m_3 - m_2} \qquad (3)$$

In addition, the shrinkage behaviour over temperature of the different powders was analysed in a horizontal push-rod type dilatometer (DIL802, Bähr GmbH) with a heating rate of 5 K/min. X-ray powder diffraction (XRD) (Ultima IV, Rigaku) with CuKα wavelength (1.5418740 Å) was used to determine the phase composition of the different powder mixtures and of the sintered samples. The microstructures of the sintered specimens were analysed on polished and fractured surfaces with scanning electron microscopy (SEM) (Gemini Supra 40, ZEISS) equipped with energy-dispersive X-ray diffraction (EDX) (NSS 3.1, Thermo). The pores and grains were analysed with the imaging software PixelFerber. Pores were classified in the micrographs according to their grey value (polished surface, with SE detector). For each synthesis condition, at least 3000 pores were analysed. To examine the grain size of the sintered specimens, the maximum Feret diameters of at least 300 grains were measured (thermally etched surface, with SE detector).

The electrical conductivity σ was calculated according to Equation (4), taking into account the distance of the inner test probes d, the height h, the width w, and the electrical resistance R. At room temperature, R of the test bars was measured with a 4-probe method using a digital multimeter (3458A, Hewlett Packard). The measurements were repeated four times for each test bar with changing current direction.

$$\sigma = \frac{d}{R \cdot h \cdot w} \qquad (4)$$

A laboratory setup was used to determine the Seebeck coefficient S at room temperature. Peltier elements cooled and heated the ends of the test bars to establish a temperature difference between +4 K and -4 K between both ends of the test probes. Thermocouples type K with bare welded tips (0.2 mm) were used as test probes to simultaneously measure the temperature difference dT and the thermovoltage U using a thermocouple data logger (TC-08, PicoLog) and a digital multimeter (8808A, Fluke), respectively. The recorded voltage values were plotted against the temperature difference. The data were fitted with a linear regression with least square method according to:

$$U = \left(S_{\text{Test bar}} + S_{\text{Chromel}}\right) \cdot dT \qquad (5)$$

with $S_{\text{Chromel}} = 22.4\ \mu\text{V/K}$ [32].

The resistance and the Seebeck coefficient of the samples were simultaneously measured as a function of temperature between 100 °C and 900 °C in a tubular furnace in synthetic air. The sliced and on-one-side-polished samples were contacted on the polished side with two platinum wires as outer electrodes. To measure both the temperature difference and the thermovoltage, two platinum-gold thermocouples were contacted as inner electrodes using a commercial platinum paste (LPA 88 – 11S, Heraeus). Subsequently, the platinum paste was fired at 950 °C for 20 min. A digital multimeter (Keithley 2700) was used to measure the resistance and the thermovoltage. The samples' resistances were measured using the four-probe dc technique in the offset compensated mode. The electrical conductivities were calculated by Equation (4). The thermovoltage of the specimens was measured while an alternating temperature gradient was created over the sample. This temperature gradient was obtained by applying a sinusoidal signal to a heater that is placed in front of the sample with a period of 100 s using a function generator (HMF 2525, Rohde & Schwarz). The thermovoltage U was plotted for each temperature step versus the temperature difference ΔT and S was calculated as explained above. Since platinum contacts and wires were used, the Seebeck coefficient of sample was corrected according to Equation (5) using the Seebeck coefficient of platinum S_{Pt} instead of S_{Chromel}. For more details about measurement setup and calculation of the Seebeck coefficient, the reader is referred to reference [33].

The thermal conductivity κ was calculated according to Equation (6) using the thermal diffusivity a, the heat capacity c_p, and the density ρ.

$$\kappa = a \cdot c_p \cdot \rho \qquad (6)$$

Thermal diffusivity a was measured using the laser flash diffusivity technique (LFA 457, Netzsch) from room temperature to 700 °C in air. The thermal diffusivity measurement was performed three times at each temperature for all specimens. The heat capacity c_p of the materials was measured from room temperature to 700 °C, with a heating rate of 20 $K \cdot min^{-1}$ in platinum crucibles in nitrogen atmosphere, using differential scanning calorimetry (STA 449 F3 Jupiter, Netzsch).

The acquired data were tested for significant differences in variance and mean value by F-test and 2-sample-t-test with the statistics package Minitab 17, respectively. The level of significance was set to 5 %.

III. Results

The thermal analysis (see Fig. 1) of the raw material mixture shows five main peaks. A maximum in mass loss is represented by a local minimum in the dTG curve in Fig. 1. The mass loss curve is not shown in Fig. 1, instead the

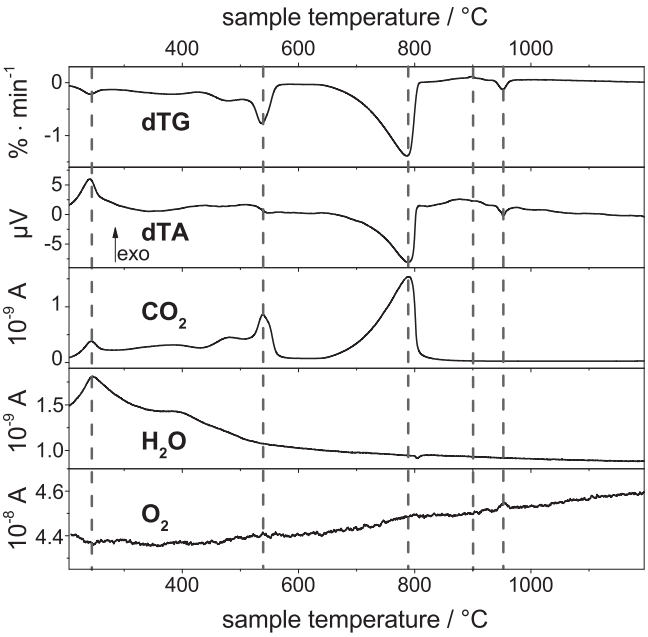

Fig. 1: Decomposition and reaction of powder mixture of $CaCO_3$, $MnCO_3$, and $Sm(OH)_3$ investigated with differential thermogravimetry (dTG), differential thermal analysis (dTA) and coupled mass spectrometry.

corresponding mass loss data are given in the text. The first mass loss peak of -3 wt% has its maximum at 240 °C. It is an exothermic reaction accompanied by a CO_2 and H_2O release. The second mass loss peak of -10 wt% has its onset at 430 °C and a maximum at 540 °C. It is characterized by a reaction with CO_2 release. The third peak is endothermic (ϑ_{onset} = 720 °C, ϑ_{max} = 790 °C) and represents a mass loss of -20 wt% by CO_2 release. Between 820 °C and 940 °C, an exothermic mass gain of 1.4 wt% was recorded. Finally, an endothermic mass loss peak was found at 950 °C accompanied by a small O_2 release.

As shown in Fig. 2, different calcination conditions led to the formation of different phases. The uncalcined powder consists of the raw materials $CaCO_3$ (PDF: 05 – 0586), $MnCO_3$ (PDF: 44 – 1472) and $Sm(OH)_3$ (PDF: 83 – 2036). Calcination at 850 °C twice leads to the formation of $CaMnO_3$ (PDF: 89 – 0666) as a main phase with secondary phases identified as Ca_2MnO_4 (PDF: 24 – 1194) and Sm_2O_3 (PDF: 15 – 0813). After calcination at 1050 °C twice, $CaMnO_3$ was identified as the main phase and $Ca_4Mn_3O_{10}$ (PDF: 89 – 0815) as a minor phase. According to XRD, all the different powder synthesis conditions led to the formation of pure $CaMnO_3$ after sintering. No secondary phases could be identified. As shown in Fig. 2 and Table 1, the particle size of the ball-milled calcined powder increased from d_{50} = 1.5 μm to d_{50} = 2.6 μm by increasing the calcination temperature from 850 °C to 1050 °C, the calcination cycles do not have a significant influence on the particle size of the calcined powder.

Two examples of microstructures of sintered test bars are shown in Fig. 3 a-b). The grain size after sintering is in the range between d_{25} = 1.3 μm and d_{75} = 2.4 μm. The calcination conditions do not affect the grain size distribution after sintering. As shown in Table 1, sintered test bars from uncalcined powder have a mean pore size area of 1 μm² and a total porosity of 18 %. The mean pore size area increases to 2 μm² if calcined powder (twice, at 1050 °C) is used, the total porosity increases as well.

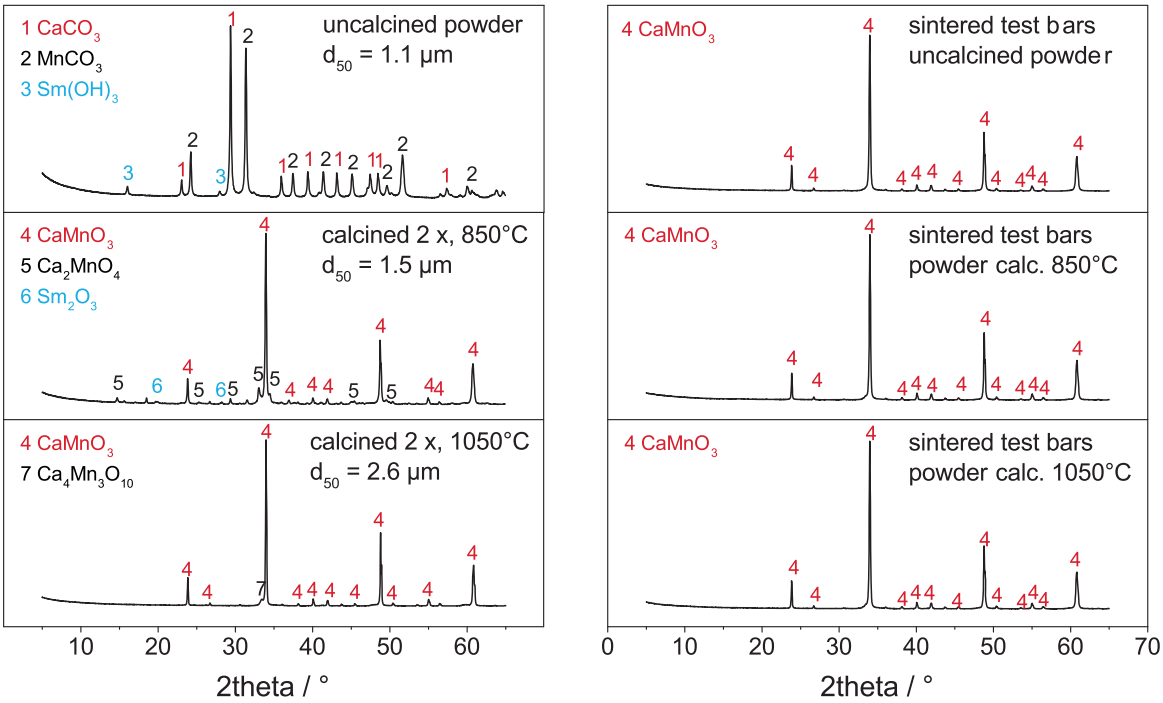

Fig. 2: XRD pattern of powder with varied calcination conditions before sintering (left side) and after sintering (right side). The particle size of the synthesized powders before sintering was determined by means of laser powder diffraction.

Table 1: Physical properties of the used powder and the sintered test bars. Particle size of the powder was measured with the diffraction method, apparent sinter density and porosity were measured with the Archimedes method, pore size and grain size by analysing the SEM micrographs. Mean values are given followed by the standard deviations.

	Uncalcined	Calcined 850 °C, 1 x	Calcined 850 °C, 2 x	Calcined 1050 °C, 2 x
Particle size powder D_{50} in µm	1.1	1.5	1.5	2.6
Grain size microstructure $D_{50,ferret}$ in µm	2.0 ± 0.8	1.9 ± 0.9	2.0 ± 0.8	1.9 ± 0.7
Sinter density in g/cm³	3.78 ± 0.03	3.50 ± 0.04	3.63 ± 0.07	3.44 ± 0.04
Porosity in %	17.4 ± 0.6	23.5 ± 0.8	20.8 ± 1.5	24.9 ± 0.8
Pore size in µm²	1.0 ± 0.1	1.9 ± 0.1	1.3 ± 0.2	2.0 ± 0.1

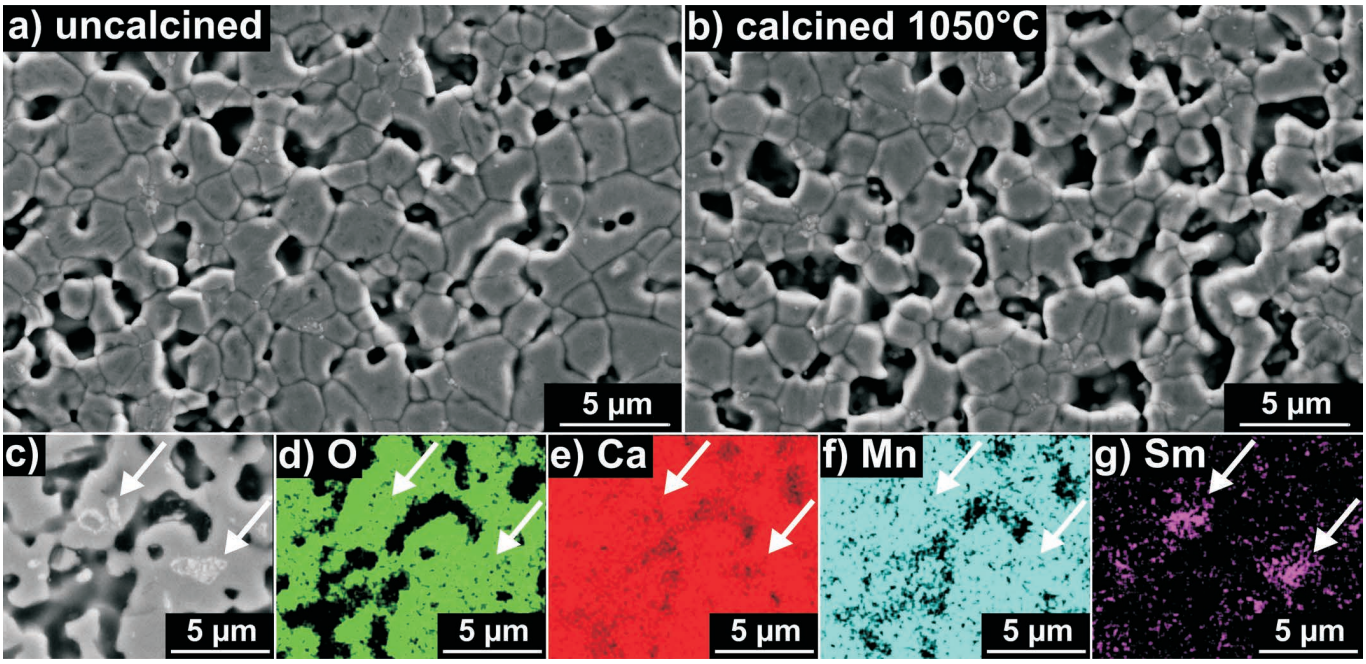

Fig. 3 a-b): SEM micrograph with SE detector from sintered and thermally etched $CaMnO_3$ from uncalcined powder and from powder calcined at 1050 °C, respectively; **c)** SEM micrograph with in-lens detector from sintered $CaMnO_3$ (polished surface) from powder calcined at 1050 °C, Sm-rich areas marked with arrows, **d-g)** corresponding EDX-mappings for O in green, Ca in red, Mn in blue, Sm in magenta.

Fig. 3 c) shows an exemplary micrograph of a polished surface with light grey areas (marked with an arrow) in a grey matrix and dark grey pores. The corresponding EDX-mapping is shown in Fig. 3 d-g). The grey matrix contains both Ca and Mn as well as a smaller amount of Sm (0.2 mol% according to quantitative analysis of EDX-spectra). The light grey areas are enriched with Sm (4.5 mol% according to quantitative analysis of EDX-spectra) and slightly Ca-deficient. Such compositional inhomogeneities are found for all tested synthesis conditions. The different synthesis conditions do not affect the area fraction of the Sm-rich areas.

Test bars from uncalcined powders show an increased shrinkage compared to the test bars from calcined powders as shown in Fig. 4. The shrinkage of specimens from uncalcined powder starts at 630 °C. The corresponding shrinkage rate shows two maxima (maxima in the shrinkage rate are minima in the displayed shrinkage rate curve in Fig. 4), one at 900 °C and one at 1175 °C. At 1200 °C, a linear shrinkage of 24 % is observed. The shrinkage rates of the specimens from calcined powder do not show any maxima. For all three test bars from calcined powders, the highest shrinkage rate is reached at the maximum temperature of 1200 °C. For the test bar prepared from powder calcined once at 850 °C, the shrinkage starts at 932 °C and reaches 10 % at 1200 °C. Two calcination cycles at 850 °C lead to a similar dilatometer curve with 945 °C as sinter starting temperature and a maximum shrinkage of 9.5 %. The specimens from powder calcined twice at 1050 °C exhibit the smallest shrinkage (1.8 % at 1200 °C) and the highest sinter start temperature of 1012 °C within the tested synthesis conditions.

As shown in Fig. 5, reaction-sintered test bars (meaning the test bars from uncalcined powder) show the highest linear shrinkage of 34 % and the highest relative sinter density of 82 %. Higher calcination temperatures and repeated calcinations lead to decreased linear shrinkage. Test bars from powders calcined at 1050 °C show only

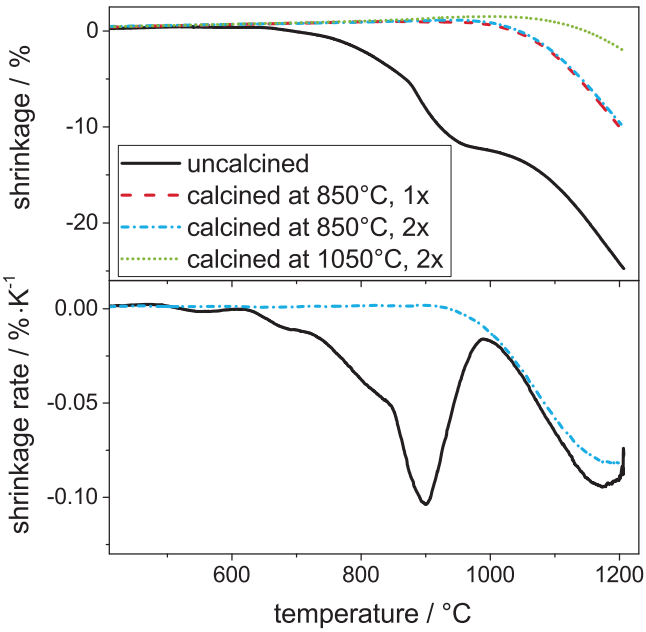

Fig. 4: Shrinkage and shrinkage rate as function of temperature for test bars prepared under different powder synthesis conditions; shrinkage curves in bold.

13 % shrinkage, which is less than half of the shrinkage of the reaction-sintered test bars. As shown in Table 1, the sinter density only amounts to 3.4 g/cm³, which is equal to $\rho_{rel} = 74$ %. The number of calcination cycles neither influences significantly the Seebeck coefficient at room temperature nor the electrical conductivity or the power factor (2-sample-t-test). Test bars from powder calcined at 1050 °C exhibit an *S* of -209 µV/K at room temperature, which is only 4 % lower than the value of reaction-sintered test bars (please note: low *S* values are favourable for n-type thermoelectrics). In contrast, the room temperature electrical conductivity of test bars from uncalcined powder is 130 % higher than of test bars with powder calcined at 1050 °C. Thus, the power factor (at room temperature) of reaction-sintered test bars is the highest within the tested calcination conditions ($PF = 230$ µW/K²m at room temperature). Calcination at 850 °C leads to samples with a lower *PF* of about 165 µW/K²m at room temperature. Moreover, for the highest calcination temperature a power factor of 107 µW/K²m was measured, which is less than half of the value from reaction-sintered test bars. Compared to twice-calcined powder, the room temperature power factors of test bars from uncalcined and once-calcined powder show a higher variance.

As shown in Fig. 6, the Seebeck coefficients at elevated temperatures of reaction-sintered test bars (black open squares) and sintered test bars from two times calcined powder at 1050 °C (red dots) do not show a significant difference (2-sample-t-test). For both synthesis conditions, the Seebeck coefficient *S* shows a minimum at 500 °C, with -230 µV/K for uncalcined powder and -250 µV/K for calcined powder (please note that lower *S* leads to a better performance). The measured values correspond well to data obtained from the literature for the same dopant and same doping level (blue triangles) [13]. The variance of specimens from uncalcined powder is significantly higher than the variance of specimens from calcined powder (F-test). The electrical conductivity undergoes a minimum at 500 °C for both synthesis conditions ($\sigma = 27$ S/cm for uncalcined and $\sigma = 15$ S/cm for calcined powder). The highest electrical conductivity is found at 900 °C ($\sigma = 43$ S/cm for uncalcined and $\sigma = 35$ S/cm for calcined powder). At lower temperatures, the difference between specimens from uncalcined and calcined powder is higher (at 100 °C: $\sigma_{uncalc.} = 1.9 \times \sigma_{calc.}$) compared to elevated temperatures (at 900 °C: $\sigma_{uncalc.} = 1.2 \times \sigma_{calc.}$).

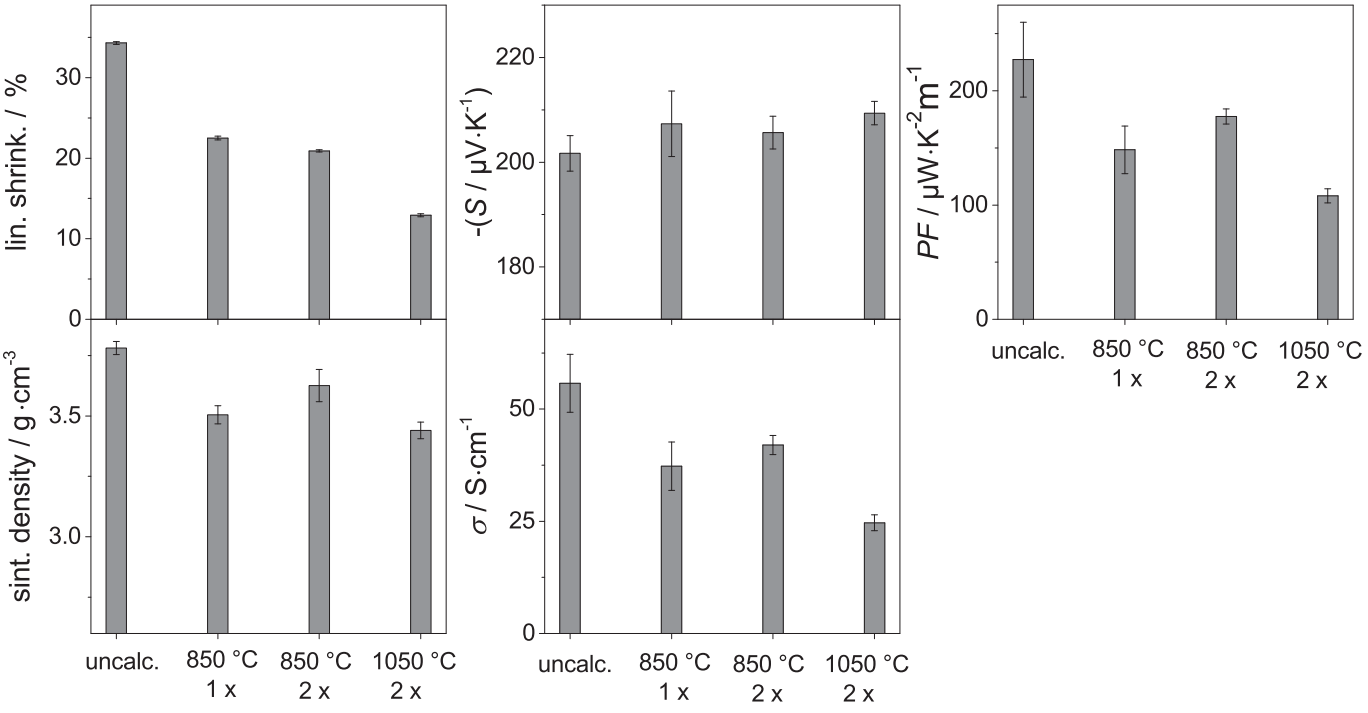

Fig. 5: Physical and thermoelectric properties at room temperature for different synthesis conditions, error bars show the corresponding standard deviations.

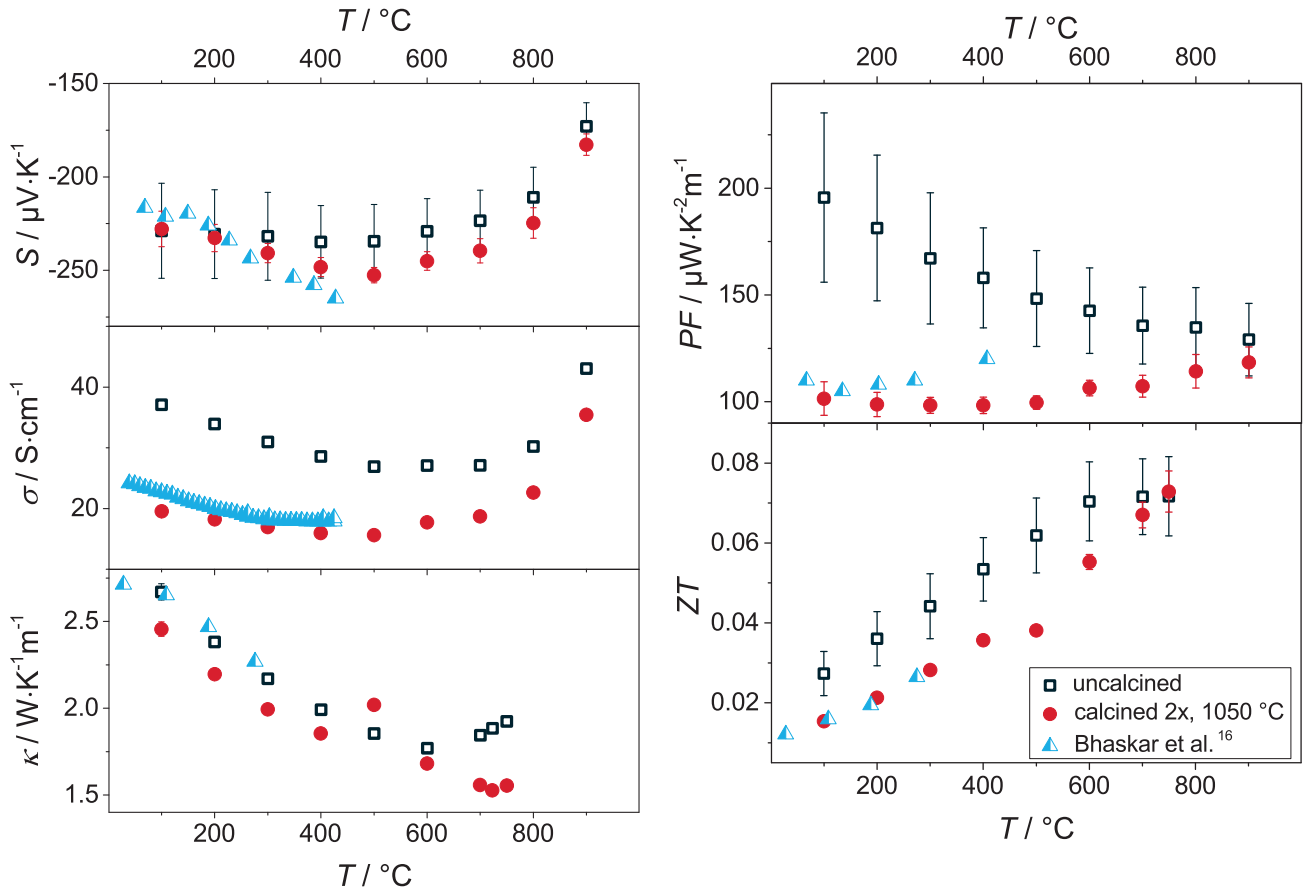

Fig. 6: Thermoelectric properties at elevated temperatures for sintered test bars from uncalcined powder and powder calcined twice at 1050 °C. Error bars indicate the standard deviation for Seebeck coefficient *S*, electrical conductivity σ, and power factor *PF*. Error bars of thermal conductivity κ and *ZT* indicate the error according to the Gaussian error propagation. Blue triangles represent data for $CaMnO_3$ doped with 0.02 mol Samarium, calcined at 900 °C for 10 h and 1200 °C for 20 h and then sintered at 1200 °C for 20 h taken from Bhaskar et al. [13].

The electrical conductivity of the test bars from calcined powder is in the same range as the values published in the literature [13]. The thermal conductivity decreases with increasing temperatures (up to 600 °C) for both synthesis conditions. Above 700 °C, the thermal conductivity increases slightly. The thermal conductivity of the reaction-sintered test bars is 8 % higher between 100 °C and 400 °C and 20 % higher above 700 °C than the thermal conductivity of test bars from calcined powder, respectively. The variance of the *PF* is significantly higher for the specimens from uncalcined powder than for the ones from calcined powder (F-test). The power factor of reaction-sintered test bars decreases with increasing temperature (from $PF = 195\ \mu W/K^2m$ at 100 °C to $PF = 130\ \mu W/K^2m$ at 900 °C). The *PF* of the specimens from calcined powder remains more or less constant between 100 °C and 500 °C ($PF \approx 100\ \mu W/K^2m$) and increases above 600 °C until it reaches approximately the same level at 900 °C as the *PF* of the reaction-sintered specimens ($PF = 120\ \mu W/K^2m$). The resulting dimensionless figure of merit *ZT* increases with increasing temperature for both synthesis conditions. At 100 °C, the figure of merit of reaction-sintered specimens is 80 % higher than the figure of merit of specimens from calcined powder. Up to 600 °C, the absolute difference in the figure of merit between the two synthesis conditions is in the range between 0.01 and 0.02. At 700 °C, both samples show the same figure of merit value of about $ZT \approx 0.07$.

IV. Discussion

The decomposition of the raw materials $CaCO_3$ and $MnCO_3$ as well as the phase formation of $CaMnO_3$ can be retraced based on the thermal analysis and mass spectroscopy data in Fig. 1. The physical water of the raw materials should be evaporated above 100 °C, corresponding well with the first dTG peak associated with a peak in the water signal. Besides, $Sm(OH)_3$ dissociates into Sm_2O_3 and H_2O from 220 °C up to about 800 °C [34], which could explain the decline in the H_2O-signal from 150 °C up to 550 °C. The decomposition of $MnCO_3$ in air to MnO_2 and CO_2 starts around 185 °C [35]. According to Berbenni *et al.* [29] $MnCO_3$ and oxygen form Mn_2O_3 and CO_2 up to 550 °C. Thus, the decomposition of $MnCO_3$ corresponds well with the first and second mass loss peak both associated with CO_2 release as described in the result section. The third mass loss peak at around 800 °C with a large signal in the CO_2-signal matches with the decomposition of $CaCO_3$ into CaO and CO_2 [36]. All decomposition reactions already minimize the chemical potential of the powder mixture. The mass gain between 820 °C and 940 °C (fourth peak) could originate from O_2 uptake from the surrounding atmosphere during the formation of $CaMnO_3$ which further reduces the chemical potential of the raw material mixture (see Equation (7)). The mass loss of O_2 at about 950 °C probably originates from the for-

mation of oxygen vacancies in $CaMnO_3$ as described, for example, by Reimann [17].

The ring-shaped accumulation of Sm in the EDX-mapping (see Fig. 3c-g) indicates an uneven incorporation of Sm into the $CaMnO_3$ lattice. A doping of 0.02 mol Sm should lead to an incorporation of 0.4 mol% Sm into $CaMnO_3$ lattice. According to the quantitative analysis of the EDX-spectra of the dark grey area (matrix) only 0.2 mol% were incorporated into the lattice, which indicates the formation of $Ca_{0.99}Sm_{0.01}MnO_3$ instead of $Ca_{0.98}Sm_{0.02}MnO_3$. The ring-shaped accumulations probably originated from former $Sm(OH)_3$ particles. Such accumulations of dopants were already described by Löhnert *et al.* [2] for the mixed-oxide route. By using soft-chemistry methods, such inhomogeneities may be avoided as the dopant is distributed more evenly [2].

The calcination conditions do not affect the Seebeck coefficient largely. *S* is a material property, mainly dependent on the charge carrier concentration and the effective density of states [37]. It can be varied, for example, by changing the doping level [20] or by reducing the oxygen partial-pressure of the sintering atmosphere [33], but this was not studied here. It has been shown for many materials that the Seebeck coefficient itself does not depend on the morphology of the samples, i.e. grain sizes, porosities or abrasive damage should not affect the Seebeck coefficient [38–40]. This is exactly what can be confirmed here as well.

In theory, repeated calcinations with an intermediate milling should improve the incorporation of the dopant in the $CaMnO_3$ lattice. This would increase the charge carrier concentration and thus decrease the electrical resistance and the absolute Seebeck value. Sm-accumulations in the microstructure should be minimized. Within the experimental framework, repeated calcinations did not affect the Sm-accumulations in the microstructure. The Seebeck coefficient and the electrical conductivity at room temperature did not differ significantly (2-sample t-test) between one calcination cycle and two calcination cycles (see Fig. 5). The only indication of an improved and more even incorporation of the Sm after two calcination cycles could be the reduced variances in electrical conductivity and Seebeck coefficient (F-test). Repeated calcinations do not seem to improve the dopant incorporation as effectively as soft chemistry methods.

When the properties of the reaction-sintered test bars are compared with the properties of the test bars from powder calcined twice at 1050 °C, large differences can be observed. Compared to the thermoelectric properties obtained from samples made from calcined powders, uncalcined powder yields samples showing higher linear shrinkage (see Fig. 4), higher sinter density with smaller pores (see Fig. 3 and Table 1), higher electrical conductivity (see Fig. 5 and Fig. 6), higher power factor (up to 700 °C, see Fig. 6), higher thermal conductivity (see Fig. 6), and consequently a higher resulting figure of merit (up to 600 °C, see Fig. 6). This can be explained by the different driving forces for sintering, regarding the different powder synthesis routes. Generally, the driving force for sintering is a combination of minimizing surface energy, minimizing lattice defects, and to some extent the reduction of chemical potential [41]. The shrinkage curve of the reaction-sintered test bars shows two maxima (see Fig. 4). Combining the results from thermal analysis and dilatometry, it can be concluded that the shrinkage of the specimens from uncalcined powder begins when $MnCO_3$ decomposes into Mn_2O_3 and CO_2 (second mass loss peak in Fig. 1). The first maximum in the shrinkage curve at 900 °C corresponds well with the decomposition temperature of $CaCO_3$ (third mass loss peak in Fig. 1). When both oxides for the formation of $CaMnO_3$ are abundant, the highest amount of $CaMnO_3$ is formed. This leads to a maximum in the shrinkage rate. Therefore, it can be assumed that the main driving force for sintering for the first peak is the reduction of the chemical potential by the formation of $CaMnO_3$ according to Equation (7).

$$CaCo_3 + MnCO_3 + 0.5\,O_2 \rightarrow CaMnO_3 + CO_2 \qquad (7)$$

After the formation of $CaMnO_3$, the sintering above 900 °C is mainly driven by minimizing lattice defects and surface energy of the particles. The second maximum in the shrinkage rate in Fig. 4 can be associated with these two mechanisms. Owing to the high driving force for sintering (minimizing lattice defects, surface energy, and chemical potential) reactive-sintering leads to the highest sinter density (see Fig. 5) within the experimental setup. In contrast, the shrinkage rate curves of test bars from calcined powder do not show the first maximum as $CaMnO_3$ was already formed during the calcination by reducing the chemical potential of the powder mixture. Therefore, the driving force for sintering of calcined powder is lower than it is for uncalcined powder. In addition, the calcination process triggers surface diffusion, which promotes grain growth (see Fig. 1) by minimizing lattice defects and surface energy [42]. This diffusion process is enhanced by higher calcination temperatures and longer dwell times. It further minimizes the driving force for sintering of the calcined powder and leads to a less densified microstructure after sintering (see Fig. 3 and Table 1). Therefore, the shrinkage rates of the specimens from calcined powder do not show any maxima. The shrinkage rate maximum due to the minimization of lattice defects and surface energy of the particles is shifted to temperatures above 1200 °C and thus is not displayed in Fig. 4. The higher the calcination temperature, the lower are the linear shrinkage and sinter density (see Fig. 4 and Fig. 5). $CaMnO_3$ shows a similar behaviour regarding uncalcined and calcined powder as recently reported for $Ca_3Co_4O_9$ [31] and $CuAlO_2$ [43]. The scheme in Fig. 7 illustrates the influence of the energy input during calcination on the driving force for sintering. As the true curve shape and the exact contribution of the different driving forces for sintering (minimizing lattice effects, surface energy and chemical potential) are very speculative, the shown diagram is only a simplified visualization of the different effects.

As shown in Fig. 8, a higher density of the sintered test bars leads to higher electrical conductivity. The correlation can even be fitted with a linear regression (R^2(adj.) = 91 %). At higher densities, porosity and pore size area are reduced and intergranular contacts are larger. This enhances the charge carrier transport and therefore increases the electrical conductivity, but as written above, this does not

affect the Seebeck coefficient. Therefore, the power factor also increases with higher density. There are different ways to increase the sinter density. First, the green density can be increased by using e.g. higher compaction pressures as reported by Zhu *et al.* [44]. Second, it is possible to sinter at higher temperatures for longer dwell times [11, 16, 18, 44], which increases the energy demand during fabrication. Finally, a powder with a high driving force for sintering is favourable to obtain high sinter densities. As written above, calcination minimizes the driving force for sintering of the powder as surface diffusion leads to grain growth, lower surface energy and fewer lattice defects [42]. To increase the driving force of the calcined powder, it is common practice to fine-mill the calcined powder over many hours [2, 14, 16, 44] or to use high-energy ball milling [29], which is again very energy intensive. In this study, it is shown that reactive sintering and calcination at lower temperatures are another effective way to increase the driving force for sintering, by lowering the energy input at the same time. Within this study, the highest power factor and figure of merit (see Fig. 5 and Fig. 6) for Sm-doped $CaMnO_3$ were obtained for reactive-sintering of the raw materials, without any calcination procedure. This leads to the assumption that although it is common practice to calcine at high temperature for a long time [2, 5, 11, 13, 16, 19, 27–30], for a good thermoelectric performance (high *PF*, high *ZT*) such a high energy input during calcination is not favourable.

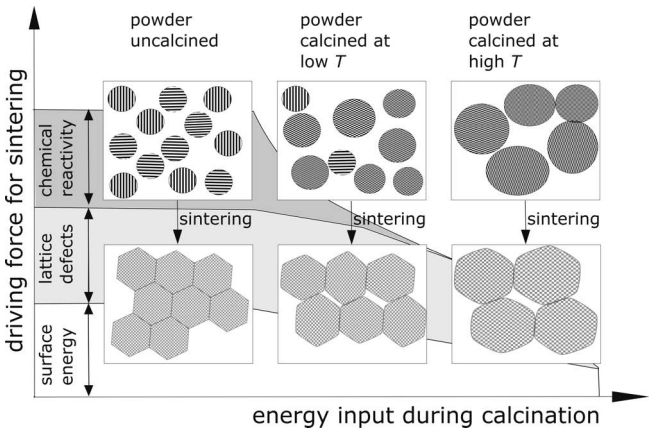

Fig. 7: Scheme of the densification behaviour for the different calcination procedures that can be explained by the driving forces for sintering. Raw materials with stripes pattern, $CaMnO_3$ with chess pattern.

As shown in Fig. 6, the electrical conductivity shows a metallic behaviour over temperature ($d\sigma/dT < 0$) for reaction-sintered specimens as well as for specimens from calcined powder up to 500 °C. The metallic behaviour is more pronounced for higher electrical conductivity. Above 700 °C, the behaviour changes to semiconducting ($d\sigma/dT > 0$), that is increasing electrical conductivity with increasing temperature. Such a behaviour change from metallic to semiconducting has already been reported for Nb-doped $CaMnO_3$ [45] and Ta-doped $CaMnO_3$ [46], but not for Sm-doped $CaMnO_3$ [13, 18–20, 27]. Doped $CaMnO_3$ shows a converse transition from semiconducting to metallic behaviour (transition temperature denoted T_{MI}) around room temperature which is well described in the literature [17, 47]. Below T_{MI} the semiconducting behaviour is described as originating from thermally activated small-polaron hopping between M^{3+} to M^{4+} states of the dopants. At the transition temperature (T_{MI}) from semiconducting to metallic, the electrons become dominant as charge carriers and the number of polarons decreases [47]. It could be concluded that the reported transition from metallic to semiconducting behaviour at around 500 °C (see Fig. 6) is the reverse effect and a second $T_{MI,2}$, where the dominant charge carrier changes from electrons to thermally activated small-polaron hopping.

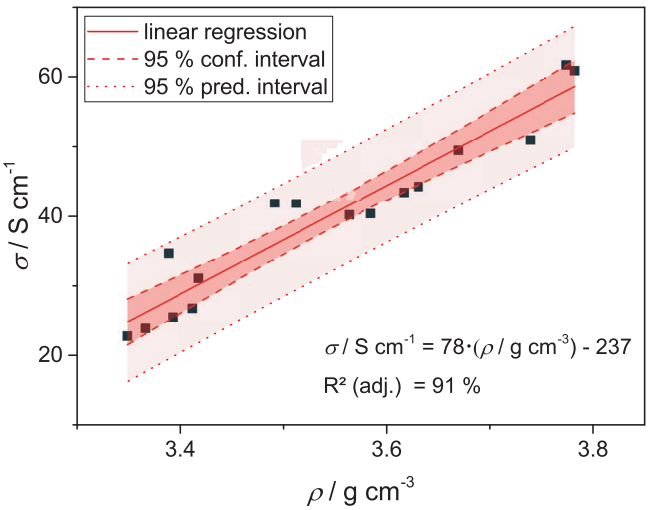

Fig. 8: Electrical conductivity at room temperature as a function of apparent density with linear regression, 95 % confidence interval and 95 % prediction interval.

Owing to the relatively low sinter temperature (1250 °C in this study compared to 1300 °C [11, 44], 1350 °C [19] and 1450 °C [16] elsewhere), short dwell time (2 h in this study to over 10 h [11, 13, 44]) and micrometre-scale powders (not fine-milled [2, 14, 16, 44]), the obtained sinter densities are relatively low (from 75 % to 83 %) compared to the values published in the literature [11, 14, 17, 44]. As shown in Fig. 8, an increased sinter density should be favourable for higher electrical conductivities and higher *PF*. The measured power factors and figures of merit are in the middle range of the values published in the literature for $CaMnO_3$ doped with various elements [1, 2, 11, 13, 17–19, 44]. As shown in Fig. 6, the high-temperature thermoelectric properties of the test bars from calcined powder correspond well with the values published in literature for $CaMnO_3$ with the same dopant samarium, same doping level and similar powder synthesis [13]. Reactive-sintering increases the electrical conductivity and thus leads to significantly higher power factors and figures of merit at higher temperatures as published in literature for Sm-doped $CaMnO_3$ [13] with the same doping level of 0.02 mol. Higher doping levels as cited in the introduction [11, 19], soft chemistry powder synthesis [20] or other dopants [2, 17, 44] may eventually lead to higher thermoelectric properties. It is very likely that fine milling, optimized dopants or higher sintering temperatures would further increase the thermoelectric properties of reaction-sintered $CaMnO_3$. Nevertheless, reaction-sintering is a method to increase the thermoelectric

properties and to decrease production costs at the same time.

V. Summary

The influence of the calcination temperature and the number of calcination cycles on the properties of $CaMnO_3$ was studied. The calcination procedure did not affect the phase content of the sintered specimens, but influenced largely sinter density, shrinkage, pore size, and thermoelectric properties. Sintered test bars from uncalcined powder performed best in respect of the thermoelectric properties in the temperature range from 22 °C to 600 °C ($PF \approx 230\,\mu W/mK^2$ at 22 °C, $PF \approx 140\,\mu W/mK^2$ at 600 °C, $ZT \approx 0.07$ at 600 °C) within the examined parameter settings. The calcination procedure barely affected the Seebeck coefficient. Repeated calcinations and higher calcination temperatures resulted in decreased thermoelectric properties and shrinkage. The electrical conductivity correlated almost linearly with the sinter density. Therefore, a powder with large driving force for sintering should be used to reach high electrical conductivity. Thermal processes that cause grain growth without densification should not be used during powder synthesis. $CaMnO_3$ can be synthesized efficiently by means of direct reactive-sintering of raw materials, without any additional calcination procedure. Thereby, the energy demand for the powder synthesis is reduced. This is an important step towards cost-effective production of thermoelectric generators using thermoelectric oxide materials.

Acknowledgments

The authors are very grateful to the BAM colleagues S. Benemann for the SEM micrographs, C. Selleng for XRD analyses, T. Marcus for the electrical conductivity setup, S. Reinsch for dTA measurement, F. Lindemann for analysing the particle size distribution, and W. Guether for the helpful advice concerning powder synthesis and specimen preparation. We also want to thank F. Giovannelli from Université de Tour for help with the thermal conductivity measurements.

References

1 Fergus, J.W.: Oxide materials for high temperature thermoelectric energy conversion, *J. Eur. Ceram. Soc.,* **32**, 525 – 540, (2012).

2 Löhnert, R., Stelter, M., Töpfer, J.: Evaluation of soft chemistry methods to synthesize Gd-doped $CaMnO_{3-\delta}$ with improved thermoelectric properties, *Mater. Sci. Eng., B,* **223**, 185 – 193, (2017).

3 Funahashi, S., Guo, H., Guo, J., Baker, A.L., Wang, K., Shiratsuyu, K., Randall, C.A.: Cold sintering and co-firing of a multilayer device with thermoelectric materials, *J. Am. Ceram. Soc.,* **100**, 3488 – 3496, (2017).

4 Delorme, F., Martin, C.F., Marudhachalam, P., Guzman, G., Ovono, D.O., Fraboulet, O.: Synthesis of thermoelectric $Ca_3Co_4O_9$ ceramics with high ZT values from a $Co^{II}Co^{III}$-layered double hydroxide precursor, *Mater. Res. Bull.,* **47**, 3287 – 3291, (2012).

5 Koumoto, K., Funahashi, R., Guilmeau, E., Miyazaki, Y., Weidenkaff, A., Wang, Y., Wan, C., Zhou, X.D.: Thermoelectric ceramics for energy harvesting, *J. Am. Ceram. Soc.,* **96**, 1 – 23, (2013).

6 Ohta, S., Nomura, T., Ohta, H., Koumoto, K.: High-temperature carrier transport and thermoelectric properties of heavily La- or Nb-doped $SrTiO_3$ single crystals, *J. Appl. Phys.,* **97**, 034106, (2005).

7 Moos, R., Gnudi, A., Härdtl, K.H.: Thermopower of $Sr_{1-x}La_xTiO_3$ ceramics, *J. Appl. Phys.,* **78**, 5042 – 5047, (1995).

8 Park, K., Ko, K.Y., Seo, W.S., Cho, W.S., Kim, J.G., Kim, J.Y.: High-temperature thermoelectric properties of polycrystalline $Zn_{1-x-y}Al_xTi_yO$ ceramics, *J. Eur. Ceram. Soc.,* **27**, 813 – 817, (2007).

9 Ohtaki, M., Araki, K., Yamamoto, K.: High thermoelectric performance of dually doped ZnO ceramics, *J. Electron. Mater.,* **38**, 1234 – 1238, (2009).

10 Guilmeau, E., Díaz-Chao, P., Lebedev, O.I., Rečnik, A., Schäfer, M.C., Delorme, F., Giovannelli, F., Košir, M., Bernik, S.: Inversion boundaries and phonon scattering in Ga:ZnO thermoelectric compounds, *Inorg. Chem.,* **56**, 480 – 487, (2017).

11 Ohtaki, M., Koga, H., Tokunaga, T., Eguchi, K., Arai, H.: Electrical transport properties and high-temperature thermoelectric performance of $(Ca_{0.9}M_{0.1})MnO_3$ (M = Y, La, Ce, Sm, In, Sn, Sb, Pb, Bi), *J. Solid State Chem.,* **120**, 105 – 111, (1995).

12 Taguchi, H.: High-temperature phase transition of $CaMnO_{3-\delta}$, *J. Solid State Chem.,* **78**, 312 – 3115, (1989).

13 Bhaskar, A., Liu, C.-J., Yuan, J.J.: Thermoelectric and magnetic properties of $Ca_{0.98}RE_{0.02}MnO_{3-\delta}$ (RE = Sm, Gd, and Dy), *J. Electron. Mater.,* **41**, 2338 – 2344, (2012).

14 Kabir, R., Wang, D., Zhang, T., Tian, R., Donelson, R., Teck Tan, T., Li, S.: Tunable thermoelectric properties of $Ca_{0.9}Yb_{0.1}MnO_3$ through controlling the particle size via ball mill processing, *Ceram. Int.,* **40**, 16701 – 16706, (2014).

15 Thiel, P., Eilertsen, J., Populoh, S., Saucke, G., Döbeli, M., Shkabko, A., Sagarna, L., Karvonen, L., Weidenkaff, A.: Influence of tungsten substitution and oxygen deficiency on the thermoelectric properties of $CaMnO_{3-\delta}$, *J. Appl. Phys.,* **114**, 243707, (2013).

16 Srivastava, D., Azough, F., Freer, R., Combe, E., Funahashi, R., Kepaptsoglou, D.M., Ramasse, Q.M., Molinari, M., Yeandel, S.R., Baran, J.D., Parker, S.C.: Crystal structure and thermoelectric properties of Sr-Mo substituted $CaMnO_3$: A combined experimental and computational study, *J. Mater. Chem. C,* **3**, 12245 – 12259, (2015).

17 Reimann, T., Töpfer, J.: Thermoelectric properties of Gd/W double substituted calcium manganite, *J. Alloy. Compd.,* **699**, 788 – 795, (2017).

18 Sanmathi, C.S., Takahashi, Y., Sawaki, D., Klein, Y., Retoux, R., Terasaki, I., Noudem, J.G.: Microstructure control on thermoelectric properties of $Ca_{0.96}Sm_{0.04}MnO_3$ synthesised by co-precipitation technique, *Mater. Res. Bull.,* **45**, 558 – 563, (2010).

19 Lemonnier, S.b., Goupil, C., Noudem, J., Guilmeau, E.: Four-leg $Ca_{0.95}Sm_{0.05}MnO_3$ unileg thermoelectric device, *J. Appl. Phys.,* **104**, 014505, (2008).

20 Su, H., Jiang, Y., Lan, X., Liu, X., Zhong, H., Yu, D.: $Ca_{3-x}Bi_xCo_4O_9$ and $Ca_{1-y}Sm_yMnO_3$ thermoelectric materials and their power-generation devices, *Phys. Status Solidi,* **208**, 147 – 155, (2011).

21 Matsubara, I., Funahashi, R., Takeuchi, T., Sodeoka, S., Shimizu, T., Ueno, K.: Fabrication of an all-oxide thermoelectric power generator, *Appl. Phys. Lett.,* **78**, 3627, (2001).

22 Koumoto, K., Wang, Y., Zhang, R., Kosuga, A., Funahashi, R.: Oxide thermoelectric Materials: A nanostructuring approach, *Annu. Rev. Mater. Res.,* **40**, 363 – 394, (2010).

23 Reimann, T., Bochmann, A., Vogel, A., Capraro, B., Teichert, S., Töpfer, J.: Fabrication of a transversal multilayer thermoelectric generator with substituted calcium manganite, *J. Am. Ceram. Soc.,* (2017).

[24] Teichert, S., Bochmann, A., Reimann, T., Schulz, T., Dressler, C., Udich, S., Töpfer, J.: A monolithic oxide-based transversal thermoelectric energy harvester, *J. Electron. Mater.,* **45**, 1966 – 1969, (2016).

[25] Segal, D.: Chemical synthesis of ceramic materials, *J. Mater. Chem.,* **7**, 1297 – 1305, (1997).

[26] Jaffe, B.: Piezoelectric Ceramics. Elsevier Science, London, 2012.

[27] Lemonnier, S., Guilmeau, E., Goupil, C., Funahashi, R., Noudem, J.G.: Thermoelectric properties of layered $Ca_{3.95}RE_{0.05}Mn_3O_{10}$ compounds (RE=Ce, Nd, Sm, Eu, Gd, Dy), *Ceram. Int.,* **36**, 887 – 891, (2010).

[28] Noudem, J.G., Lemonnier, S., Prevel, M., Reddy, E.S., Guilmeau, E., Goupil, C.: Thermoelectric ceramics for generators, *J. Eur. Ceram. Soc.,* **28**, 41 – 48, (2008).

[29] Berbenni, V., Milanese, C., Bruni, G., Cofrancesco, P., Marini, A.: Solid state synthesis of $CaMnO_3$ from $CaCO_3$-$MnCO_3$ mixtures by mechanical energy, *Z. Naturforsch. B,* **61**, (2006).

[30] Xu, G., Funahashi, R., Pu, Q., Liu, B., Tao, R., Wang, G., Ding, Z.: High-temperature transport properties of Nb and Ta substituted $CaMnO_3$ system, *Solid State Ionics,* **171**, 147 – 151, (2004).

[31] Bresch, S., Mieller, B., Selleng, C., Stöcker, T., Moos, R., Rabe, T.: Influence of the calcination procedure on the thermoelectric properties of calcium cobaltite $Ca_3Co_4O_9$, *J. Electroceram.,* (2018).

[32] Campari, M., Garribba, S.: The behavior of type K thermocouples in temperature Measurement: the chromel P-Alumel thermocouples, *Rev. Sci. Instrum.,* **42**, 644 – 653, (1971).

[33] Stöcker, T., Exner, J., Schubert, M., Streibl, M., Moos, R.: Influence of oxygen partial pressure during processing on the thermoelectric properties of aerosol-deposited $CuFeO_2$, *Materials,* **9**, 227, (2016).

[34] Duval, T., Duval, C.: About the gravimetry analysis of precipitates: dosing of samarium, in french, *Anal. Chim. Acta,* **2**, 228 – 229, (1948).

[35] Sabry, A.I., Mahdy, A.M., Abadir, M.F.: Thermal decomposition of $MnCO_3$ (in air), *Thermochim. Acta,* **98**, 269 – 276, (1986).

[36] Dean, J.: Lange's handbook of chemistry. 15 edition. MvGraw-Hill, Inc., New York, United States of America, 1999.

[37] Rettig, F., Moos, R.: Morphology dependence of thermopower and conductance in semiconducting oxides with space charge regions, *Solid State Ionics,* **179**, 2299 – 2307, (2008).

[38] Gerthsen, P., Härdtl, K.H., Csillag, A.: Mobility determinations from weight measurements in solid solutions of (Ba, Sr)TiO_3, *Phys. Status Solidi,* **13**, 127 – 133, (1972).

[39] Rettig, F., Moos, R.: Direct thermoelectric gas sensors: design aspects and first gas sensors, *Sensor. Actuat., B,* **123**, 413 – 419, (2007).

[40] Moos, R., Fandel, M., Schäfer, W.: High-load resistors of doped titanate ceramics showing PTCR behavior in the entire temperature range of operation, *J. Eur. Ceram. Soc.,* **19**, 759 – 763, (1999).

[41] Salmang, H., Telle, R., Scholze, H.: (Ceramics) Keramik. Springer Berlin Heidelberg, 2006, 376 – 377.

[42] Kingery, W.D., Bowen, H.K., Uhlmann, D.R.: Introduction to ceramics. Wiley, New York, 1976, 449 – 452.

[43] Liou, Y.-C., Chang, L.-S., Lu, Y.-M., Tsai, H.-C., Lee, U.-R.: Effects of mechanical milling on preparation and properties of $CuAl_{1-x}Fe_xO_2$ thermoelectric ceramics, *Ceram. Int.,* **38**, 3619 – 3624, (2012).

[44] Zhu, Y., Wang, C., Su, W., Li, J., Liu, J., Du, Y., Mei, L.: High-temperature thermoelectric performance of $Ca_{0.96}Dy_{0.02}RE_{0.02}MnO_3$ ceramics (RE=Ho, er, Tm), *Ceram. Int.,* **40**, 15531 – 15536, (2014).

[45] Bocher, L., Aguirre, M.H., Logvinovich, D., Shkabko, A., Robert, R., Trottmann, M., Weidenkaff, A.: $CaMn_{1-x}Nb_xO_3$ ($x \leq 0.08$) perovskite-type phases as promising new high-temperature n-type thermoelectric materials, *Inorg. Chem.,* **47**, 8077 – 8085, (2008).

[46] Ledezma, K.E.: The relation between microstructure and thermoelectric properties in Ta-substituted A-site deficient $CaMnO_3$. NTNU, Trondheim, 2017.

[47] Wang, Y., Sui, Y., Cheng, J., Wang, X., Lu, Z., Su, W.: High temperature Metal-Insulator transition induced by rare-earth doping in perovskite $CaMnO_3$, *J. Phys. Chem. C,* **113**, 12509 – 12516, (2009).